



**AALBORG UNIVERSITY**  
DENMARK

**Aalborg Universitet**

## **Internal Model Current Control of Brushless Doubly Fed Induction Machines**

Su, Mei; Jin, Weiyu; Zhang, Guanguan; Tang, Weiyi; Blaabjerg, Frede

*Published in:*  
Energies

*DOI (link to publication from Publisher):*  
[10.3390/en11071883](https://doi.org/10.3390/en11071883)

*Creative Commons License*  
CC BY 4.0

*Publication date:*  
2018

*Document Version*  
Publisher's PDF, also known as Version of record

[Link to publication from Aalborg University](#)

*Citation for published version (APA):*  
Su, M., Jin, W., Zhang, G., Tang, W., & Blaabjerg, F. (2018). Internal Model Current Control of Brushless Doubly Fed Induction Machines. *Energies*, 11(7), 1-19. [1883]. <https://doi.org/10.3390/en11071883>

### **General rights**

Copyright and moral rights for the publications made accessible in the public portal are retained by the authors and/or other copyright owners and it is a condition of accessing publications that users recognise and abide by the legal requirements associated with these rights.



- ? Users may download and print one copy of any publication from the public portal for the purpose of private study or research.
- ? You may not further distribute the material or use it for any profit-making activity or commercial gain
- ? You may freely distribute the URL identifying the publication in the public portal ?

### **Take down policy**

If you believe that this document breaches copyright please contact us at [vbn@aub.aau.dk](mailto:vbn@aub.aau.dk) providing details, and we will remove access to the work immediately and investigate your claim.

Article

# Internal Model Current Control of Brushless Doubly Fed Induction Machines

Mei Su <sup>1</sup>, Weiyu Jin <sup>1</sup>, Guanguan Zhang <sup>1,\*</sup> , Weiyi Tang <sup>1</sup> and Frede Blaabjerg <sup>2</sup> 

<sup>1</sup> School of Information Science and Engineering, Central South University, Changsha 410083, China; sumeicsu@csu.edu.cn (M.S.); kingweiyu@163.com (W.J.); 154601016@csu.edu.cn (W.T.)

<sup>2</sup> Department of Energy Technology, Aalborg University, DK-9220 Aalborg, Denmark; fbl@et.aau.dk

\* Correspondence: dr\_zgg@163.com; Tel.: +86-152-0089-8145

Received: 1 July 2018; Accepted: 16 July 2018; Published: 19 July 2018



**Abstract:** In the wind energy generation system, the brushless doubly-fed induction machine (BDFIM) has shown significant application potential, since it eliminates the electric brush and slip ring. However, the complicated rotor structure increases the control difficulty, especially resulting in complicated coupled terms in the current sub-system, which deteriorates the dynamic performance and reduces the system robustness. In order to address the problems caused by complex coupled terms, an internal model current control strategy is presented for the BDFIM, and an active damping term is designed for suppressing the disturbance caused by the total resistance. The proposed method simplifies the controller parameters design, and it achieves the fast-dynamic response and the good tracking performance, as well as good robustness. On the other hand, the feedforward term composed by the grid voltage is added to the internal model controller in order to suppress the disturbance when the symmetrical grid voltage sag happens. Finally, the simulation and experimental results verify the feasibility and effectiveness of the proposed method.

**Keywords:** brushless doubly-fed induction machine; current controller; internal model control; parameter estimation

## 1. Introduction

The Doubly Fed Induction Generator (DFIG) has been widely used in wind energy generation systems (WEGs), because the capability of its power converter is only about one third the wind turbine power rating [1], but the slip rings and electro-brushes of the DFIG lead to frequent maintenance and increases the system cost, especially for offshore wind farms [2]. The Brushless Doubly Fed Induction Machine (BDFIM) has the outstanding features of no slip rings and electro-brushes, resulting in more robustness and durability than the DFIG [3–5]. Furthermore, the BDFIM has two stators, denoted as the power winding (PW) stator and the control winding (CW) stator, and a special designed rotor, where the rotor has two kinds of structures as the squirrel-cage type and the wound-rotor type [6]. On the other hand, the BDFIM is equivalent to the DFIG in function, which makes the BDFIM is more attractive in terms of the WEG applications [7–9].

In terms of the BDFIM control methods, the scalar control has no feedback link and it is difficult to obtain a fast dynamic response [10]. The direct power control [11] and the indirect control scheme [12] directly regulate the speed or power by the amplitude and angle of the CW flux, while good dynamic responses are questionable due to the lack of timely current adjustment; on the other hand, direct control methods [13–15] require high switching frequency to reduce torque ripples and relies on accurate estimations of torque or flux, thus the vector control method is preferred due to simple control structure and easy implementation. In addition, the single-loop control method simplifies the control algorithm at the sacrifices of tracking performance [16], the vector control with the inner current

controller is more commonly used in drive system, where the inner current sub-system is designed as a small time constant system in order to achieve good dynamics.

In the inner current sub-system of the BDFIM, complex cross-coupling terms, the back electromotive force (EMF) disturbance and parametric errors increase the difficulty of the controller design and decrease the control performance [17–19], while the previous current control methods of the BDFIM have not addressed the problems caused by parametric errors. In addition, effects of complex coupling terms are usually eliminated or suppressed by combining the conventional PI controller and the feedforward control. Different feedforward compensation terms generate diverse total resistances and total leakage inductances of the current sub-system, which directly affect the current controller design and the control performance. In [17] the feedforward component consists of the CW flux, the PW flux, and the CW current; In [18], the PW flux, the derivative of the PW flux, the PW current and the CW current make up the feedforward component; while the feedforward terms are calculated by the PW current, CW current and their derivatives in [19]. However, these feedforward terms are very complex, and the compensation performance is guaranteed by precise motor parameters and calculations especially when the derivatives of the current are included. In addition, the above controllers are designed based on the CW resistance of the BDFIM, which is impossible to measure accurately. Simple controller is designed by neglecting the rotor resistance [20], but effects of the rotor resistance on the current controller of the BDFIM are not taken into accounts, which inevitably reduces the control performance [21–23].

In order to address the problems caused by complex coupling terms and parametric errors and enhance the robustness and dynamic responses of the current controller, an internal model current control strategy with the “active resistance” is proposed in this paper, where effects of the rotor resistance are reduced. In this method, the slow timescale dynamics of the flux sub-system are studied based on the state space mathematical model of the BDFIM, and a detailed design procedure of the current controller is discussed. Also, when the symmetrical PW voltage sag happens, an EMF feedforward term composed by the grid voltage is added in the current controller. Furthermore, the machine parameters are estimated, and the influences of erroneous parameters on the current controller are studied.

This paper is organized as follows: an introduction to the current controller of the BDFIM is discussed in Section 1. The state-space model of the BDFIM in the PW  $dq$  synchronous reference frame is introduced in Section 2, and then the dynamics of the flux sub-system is studied. A CW current controller based on the internal model control method is designed in Section 3. The BDFIM parameters are estimated and their effects on the CW current controller are studied in Section 4. Simulation and experimental results are presented in Section 5. Discussions on the feasibility of the proposed method are given in Section 6. Finally, the conclusions are derived in Section 7.

## 2. System Configuration and Mathematical Model of the BDFIM

The schematic diagram of the BDFIM system is described in Figure 1, where the BDFIM is composed of the PW stator, the CW stator, and the rotor. Usually, the harmonic orders and its components of the rotor windings of the wound-rotor type rotor BDFIM are relatively reduced, and the motor efficiency is high, thus the wound-rotor-type BDFIM is studied in this paper. However, the proposed method is also useful for the first type, because only the fundamental magnetic potential determines the controller design here. The power grid directly connects the BDFIM by the PW stator, and the transformer outputs a suitable voltage to meet the grid-connected requirement. In this system, the BDFIM is regulated by pouring the expected current into the CW stator, and these currents are generated by the power converter.

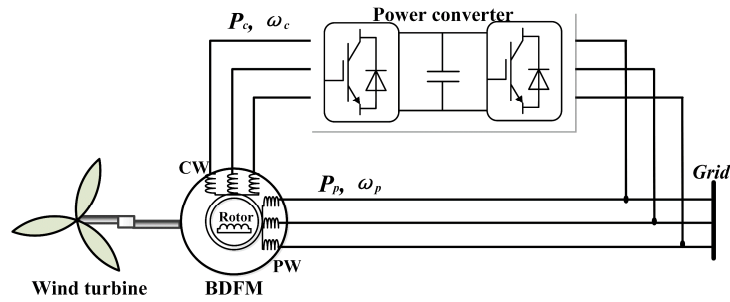


Figure 1. The schematic diagram of the brushless doubly fed induction machine system.

### 2.1. Grid-Flux Orientation

In order to realize the vector control scheme, all the quantities are oriented in the reference frame, which is aligned with a flux linkage. In terms of the DFIG system, in contrast to stator-flux orientation, the flux dynamics and system stability are independent of the rotor current by using grid-flux orientation, while they are equal in the steady state because the stator resistance is neglectable [24]. Similarly, considering the above features, the BDFIM control is discussed in the grid-flux orientation frame, the  $dq$  components of the grid-flux are  $\phi_{gd} = |\phi_g|$  and  $\phi_{gq} = 0$ , where  $\phi_{gd}$  and  $\phi_{gq}$  are the  $dq$  components of the grid-flux  $\phi_g$ . The orientation angle, denoted as  $\theta_F$ , is calculated as:

$$\theta_F = \theta_g - \frac{\pi}{2} \tag{1}$$

where  $\theta_g$  is the angle of grid voltage  $v_g$  and obtained by a phase-locked loop (PLL) estimator.

In this case, a  $dq$  synchronous reference frame is built by  $x^{dq} = e^{-j\theta_F} \vec{x}^p$  and  $x^{dq} = x^d + jx^q$ , where  $x$  is the arbitrary variable, the superscripts “ $dq$ ”, “ $d$ ”, “ $q$ ” represent the  $dq$  frame,  $d$ -axis component and  $q$ -axis component, respectively. Then, the rotor current and rotor flux are written as  $i_r^{dq} = e^{-j(\theta_F - P_p(\theta_r + \delta_1))} \vec{i}_r^{\alpha\beta r}$ ,  $\psi_r^{dq} = e^{-j(\theta_F - P_p(\theta_r + \delta_1))} \vec{\psi}_r^{\alpha\beta r}$ , where  $P_p$  is the number of pole pairs of the PW stator,  $\delta_1$  is the initial angular position between PW stator and the rotor, and  $\theta_r$  is the mechanical rotor angle. The PW and CW variables are  $x_p^{dq} = e^{-j\theta_F} x_p^{\alpha\beta p}$ ,  $x_c^{dq} = -e^{-j(\theta_F - (P_p(\theta_r + \delta_1) + P_c(\theta_r + \delta_2)))} \left( x_c^{\alpha\beta c} \right)^*$ , where “ $*$ ” represents the conjugate of the vector, the subscripts “ $p$ ” and “ $c$ ” represent the PW and the CW,  $P_c$  is the number of pole pairs of the CW stator,  $\delta_2$  is the initial angular position between CW stator and the rotor, the superscripts “ $\alpha\beta p$ ” and “ $\alpha\beta c$ ” are the stationary coordinate systems of the PW stator and the CW stator, respectively.

### 2.2. Mathematical Model of the BDFIM

On the basis of the grid-flux orientation frame, the basic mathematical model of the BDFIM [25] is expressed as:

$$v_p^{dq} = R_p i_p^{dq} + \frac{d}{dt} \psi_p^{dq} + j\omega_p \psi_p^{dq} \tag{2}$$

$$\psi_p^{dq} = L_p i_p^{dq} + M_p i_r^{dq} \tag{3}$$

$$v_c^{dq} = R_c i_c^{dq} + \frac{d}{dt} \psi_c^{dq} + j(\omega_p - (P_p + P_c)\omega_r) \psi_c^{dq} \tag{4}$$

$$\psi_c^{dq} = L_c i_c^{dq} + M_c i_r^{dq} \tag{5}$$

$$0 = R_r i_r^{dq} + \frac{d}{dt} \psi_r^{dq} + j(\omega_p - P_p\omega_r) \psi_r^{dq} \tag{6}$$

$$\psi_r^{dq} = L_r i_r^{dq} + M_p i_p^{dq} + M_c i_c^{dq} \tag{7}$$



where,  $v$ ,  $i$  and  $\psi$  are the voltage, current and flux;  $R$ ,  $L$  and  $M$  are the resistance, self-inductance and mutual inductance; the subscript “ $r$ ” represent the rotor;  $\omega_p$  and  $\omega_c$  are the electric angle frequencies of the PW stator and the CW stator, and  $\omega_r$  is the mechanical angular frequency of rotor, respectively.

Taking the CW stator current  $i_c$ , the PW stator flux  $\psi_p$  and the rotor flux  $\psi_r$  as state variables, the state-space BDFIM model is derived from Equations (2)–(7), and it is given as:

$$L_\sigma \frac{d}{dt} i_c^{dq} = -R_t i_c^{dq} - j\omega_{slc} L_\sigma i_c^{dq} + v_c^{dq} + E \quad (8)$$

$$\frac{d}{dt} \mathbf{x}_\psi = \mathbf{A}_\psi \mathbf{x}_\psi + \mathbf{B}_\psi i_c^{dq} + \begin{bmatrix} 1 & 0 \end{bmatrix}^T v_p^{dq} \quad (9)$$

where  $L_\sigma$  and  $R_t$  are the equivalent leakage inductance and equivalent total resistance;  $\omega_{slc}$  is the slip frequency of the CW stator and  $\omega_{slc} = \omega_p - (P_p + P_c)\omega_r$ ;  $\mathbf{X}_\psi$ ,  $\mathbf{A}_\psi$ , and  $\mathbf{B}_\psi$  are the state matrix, the dynamic matrix and the input matrix, and  $\mathbf{x}_\psi = \begin{bmatrix} \psi_p^{dq} & \psi_r^{dq} \end{bmatrix}^T$ ,  $\mathbf{A}_\psi = \begin{bmatrix} -a_{22} - j\omega_p & a_{23} \\ a_{32} & -a_{33} - j\omega_{slr} \end{bmatrix}$ ,  $\mathbf{B}_\psi = \begin{bmatrix} a_{21} & a_{31} \end{bmatrix}^T$ ;  $E$  is the back electromotive force and  $E = a_{12}\psi_p^{dq} + a_{13}\psi_r^{dq} + w_{11}v_p^{dq}$ ; the detailed parameters are given in Appendix A.

As shown in Equations (8) and (9), the BDFIM is a multi-variable system (containing PW stator flux, rotor flux, and the CW current), which consists of the current sub-system and the flux sub-system. In order to independently analyze and control the current sub-system, the stability of the flux sub-system is subsequently discussed.

### 2.3. Stability Analysis of the Flux Sub-System

In the flux sub-system, the poles of the system transfer function are placed at the eigenvalues of  $\mathbf{A}_\psi$ , while the system is stable when the poles are located on the left half-plane. However, it is difficult to directly obtain the poles. In this case, the Routh-Hurwitz stability criterion is adopted to estimate the range of the poles.

Usually, the Routh-Hurwitz stability criterion is used in the vector spaces with real numbers, then the matrix  $\mathbf{A}_\psi$  is transformed to  $\mathbf{A}_\psi^R$ , which is expressed as:

$$\mathbf{A}_\psi^R = \begin{bmatrix} -a_{22}\mathbf{I} - \omega_p\mathbf{J} & a_{23}\mathbf{I} \\ a_{32}\mathbf{I} & -a_{33}\mathbf{I} - \omega_{slr}\mathbf{J} \end{bmatrix} \quad (10)$$

where  $\mathbf{I} = \begin{bmatrix} 1 & 0 \\ 0 & 1 \end{bmatrix}$ ,  $\mathbf{J} = \begin{bmatrix} 0 & -1 \\ 1 & 0 \end{bmatrix}$ .

The characteristic polynomial of  $\mathbf{A}_\psi^R$  is expressed as:

$$f_1(\lambda) = \det(\lambda\mathbf{I}_2 - \mathbf{A}_\psi^R) \quad (11)$$

where  $\mathbf{I}_2 = \begin{bmatrix} \mathbf{I} & \mathbf{0} \\ \mathbf{0} & \mathbf{I} \end{bmatrix}$ .

Then, a set of four determinants is achieved from coefficients of 4th-degree characteristic polynomial Equation (11), and the coefficients used to estimate the system stability are expressed as:

$$\begin{aligned} D_1 &= 2\delta \\ D_2 &= \delta^2 + \varepsilon + \frac{a_{22}\omega_p^2 + a_{33}\omega_{slr}^2}{\delta} \\ D_3 &= \frac{2(\delta^2 + (\omega_{slr} + \omega_p)^2)(\delta^2\varepsilon + a_{22}a_{33}(\omega_p - \omega_{slr})^2)}{\delta^3 + \delta\varepsilon + a_{22}\omega_p^2 + a_{33}\omega_{slr}^2} \\ D_4 &= \varepsilon^2 + a_{22}^2\omega_{slr}^2 + a_{33}^2\omega_p^2 + 2a_{23}a_{32}\omega_p\omega_{slr} + \omega_{slr}^2\omega_p^2 \end{aligned} \quad (12)$$

where  $\delta = K_\delta(L_r R_{sp} + L_{sp} R_r)$ ,  $\varepsilon = K_\delta R_{sp} R_r$ .

Obviously, the coefficients in (12) are positive and  $D_1 > 0$ ,  $D_2 > 0$ ,  $D_3 > 0$ ,  $D_4 > 0$ , thus the stability conditions are satisfied according to the Routh-Hurwitz stability criterion, and the real parts of eigenvalues of  $\mathbf{A}_\psi^R$  are negative.

In order to estimate the range of poles of the flux sub-system, a new characteristic polynomial equation is constructed by adding  $\delta \mathbf{I}_2$  to  $\mathbf{A}_\psi^R$ , which is expressed as:

$$f_2(\lambda) = \det(\lambda \mathbf{I}_2 + (\mathbf{A}_\psi^R + \delta \mathbf{I}_2)) \tag{13}$$

The coefficients of Equation (13) are calculated as:

$$\begin{aligned} D_{21} &= 2\delta \\ D_{22} &= \delta^2 + \varepsilon + \frac{a_{22}\omega_{slr}^2 + a_{33}\omega_p^2}{\delta} \\ D_{23} &= \frac{2(\delta^2 + (\omega_{slr} + \omega_p)^2)(\delta^2\varepsilon + a_{22}a_{33}(\omega_p - \omega_{slr})^2)}{\delta^3 + \delta\varepsilon + a_{22}\omega_{slr}^2 + a_{33}\omega_p^2} \\ D_{24} &= \varepsilon^2 + a_{22}^2\omega_{sp}^2 + a_{33}^2\omega_{slr}^2 + 2a_{23}a_{32}\omega_p\omega_{slr} + \omega_{slr}^2\omega_p^2 \end{aligned} \tag{14}$$

Similarly, the new system is stable since all the coefficients in Equation (14) are positive, and the eigenvalues of Equation (13) are located on the left half-plane. Normally, the eigenvalues of  $N$  and  $-N$  are symmetric about the imaginary axis, real parts of the eigenvalues of  $\mathbf{A}_\psi^R$  are consequently larger than  $-\delta$ , and real components of the poles of flux dynamic system Equation (10) are placed between  $-\delta$  and zero on the left half-plane.

Without loss of generality, the CW current loop is designed as a high-gain feedback system, and then the DFIG system described by Equations (8) and (9) is a singularly perturbed system, where the fluxes are considered as the slowly varying variables and the current has a fast timescale dynamic. Since the flux sub-system is stable as discussed above, the current sub-system can be dependently controlled, where the fluxes are assumed in the steady-state. More details about the current controller design are given in the following part.

### 3. Design of the CW Current Controller

In the BDFIM drive system, both the power generation and rotor speed control can be achieved by properly adjusting the CW current as discussed in [22,25,26], where a well-designed current controller is a prerequisite for the normal operation of the BDFIM system. In this part, the design details of the CW current controller are discussed, which aims to track the CW current command under the disturbance of the coupling terms and BDFIM parametric errors as shown in Equation (8). In order to achieve this aim, the proposed current controller is designed based on the internal model method [27], and an active damping controller is added to increase the robustness of the system.

#### 3.1. Internal Model Current Control

By applying the Laplace transform, the current sub-system Equation (8) is expressed as:

$$Y(s) = G(s)U(s) + F_E \tag{15}$$

where  $Y(s)$  and  $U(s)$  are the system input and the system output respectively, and they are  $Y(s) = [i_{cd}(s) i_{cq}(s)]^T$  and  $U(s) = [v_{cd}(s) v_{cq}(s)]^T$ ,  $i_{cd}$ ,  $i_{cq}$ ,  $v_{cd}$  and  $v_{cq}$  are the  $d$ -axis component and  $q$ -axis component of  $i_c$  and  $v_c$ , respectively;  $G(s)$  is the controller system and

$$G(s) = \begin{bmatrix} L_\sigma s + R_t & -\omega_{slc} L_\sigma \\ \omega_{slc} L_\sigma & L_\sigma s + R_t \end{bmatrix}^{-1}; F_E \text{ is the back EMF and } F_E = a_{12} \begin{bmatrix} \psi_{pd}(s) \\ \psi_{pq}(s) \end{bmatrix} + a_{13} \begin{bmatrix} \psi_{rd}(s) \\ \psi_{rq}(s) \end{bmatrix} +$$

$w_{11} \begin{bmatrix} v_{pd}(s) \\ v_{pq}(s) \end{bmatrix}$ , where  $\psi_{pd}, \psi_{pq}, \psi_{rd}, \psi_{rq}, v_{pd}$  and  $v_{pq}$  are the  $d$ -axis component and  $q$ -axis component of  $\psi_p, \psi_r$  and  $v_p$ , respectively.

The typical internal model control diagram is shown in Figure 2,  $R(s)$  is the system input reference and  $R(s) = \begin{bmatrix} i_{cd}^{ref}(s) & i_{cq}^{ref}(s) \end{bmatrix}^T$ ,  $\hat{G}(s)$  is the internal model of the current sub-system, and  $F_{IMC}(s)$  is the equivalent current controller, where  $C_{IMC}(s)$  is the internal model controller and it is usually designed as:

$$C_{IMC}(s) = \hat{G}^{-1}(s)L_R(s) \tag{16}$$

where  $L_R(s)$  is the feedforward filter designed to enhance the controller robustness.

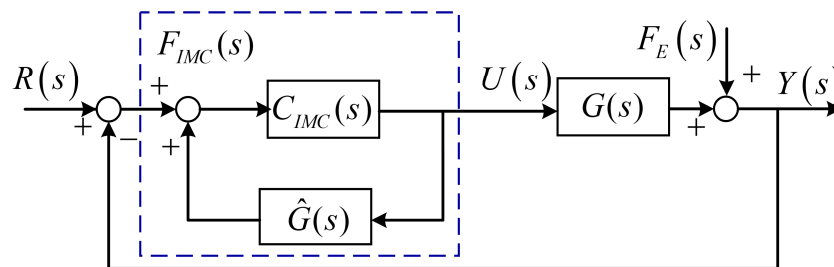


Figure 2. Schematic diagram of the internal model control method.

It can be seen from Equation (8) that the current sub-system is a first-order system, then  $L_R(s)$  is designed to be a first-order filter and it is expressed as:

$$L_R(s) = \frac{\alpha_b}{s + \alpha_b} \mathbf{I} \tag{17}$$

where  $\alpha_b$  is the desired closed-loop bandwidth of the CW current sub-system.

According to Equations (16) and (17), the equivalent current controller is designed as:

$$F_{IMC}(s) = \frac{C_{IMC}(s)}{1 - \hat{G}(s)C_{IMC}(s)} = \frac{\hat{G}^{-1}(s)L_R(s)}{1 - \hat{G}(s)\hat{G}^{-1}(s)L_R(s)} = \frac{\alpha_b}{s} \hat{G}^{-1}(s) \tag{18}$$

$$= \begin{bmatrix} K_p + \frac{K_i}{s} & 0 \\ 0 & K_p + \frac{K_i}{s} \end{bmatrix} + \begin{bmatrix} 0 & \frac{\alpha_b \omega_c \hat{L}_\alpha}{s} \\ \frac{\alpha_b \omega_c \hat{L}_\alpha}{s} & 0 \end{bmatrix}$$

where  $\hat{G}(s) = \begin{bmatrix} \hat{L}_\sigma s + \hat{R}_t & -\omega_{slc} \hat{L}_\sigma \\ \omega_{slc} \hat{L}_\sigma & \hat{L}_\sigma s + \hat{R}_t \end{bmatrix}^{-1}$ ,  $K_p = \hat{L}_\sigma \alpha_b$ ,  $K_i = \hat{R}_t \alpha_b$ , and “ $\hat{\cdot}$ ” represents the estimated value. From Equation (18), the proposed controller consists of a conventional PI controller and a decoupling controller, which is able to eliminate the effects of the uncertain disturbance by designing a proper  $\alpha_b$ , consequently the control performance is improved.

Additionally,  $R_t$  highly depends on the motor parameters, and the control performance is degraded when  $R_t$  is inaccurate. In order to improve the robustness to the parameter variations, the active damping term  $R_i$ , constructed by the feedback control of the current with a gain, is inserted in the proposed controller. When  $R_i$  is designed as  $R_i \gg R_t$ , the current is instantaneously controlled within the control bandwidth, and the current controller is robust to the variation of  $R_t$  [28]. In this paper, the active damping controller  $F_R(s)$  is expressed as:

$$F_R = \begin{bmatrix} R_i & 0 \\ 0 & R_i \end{bmatrix} = \begin{bmatrix} \hat{L}_\sigma \alpha_b & 0 \\ 0 & \hat{L}_\sigma \alpha_b \end{bmatrix} \tag{19}$$

Therefore, the proposed current controller is designed based on Equations (18) and (19). According to Figure 2, the CW stator voltage is written as:

$$U(s) = \hat{G}^{-1}(s)Y(s) - F_R Y(s) + F_{PI}(s)E_C(s) \quad (20)$$

where,  $F_{PI}(s)$  is the PI controller described as the first term in Equation (18),  $E_C(s)$  is the current tracking error and  $E_C(s) = \begin{bmatrix} i_{cd}^{ref}(s) - i_{cd}(s) \\ i_{cq}^{ref}(s) - i_{cq}(s) \end{bmatrix}$ .

From Equations (15)–(20), when the internal model is perfect and  $\hat{G}(s) = G(s)$ , the CW current is calculated as:

$$\begin{aligned} Y(s) &= L_R(s)R(s) + L_E(s)F_E(s) \\ &= \frac{\alpha_b}{s+\alpha_b}R(s) + \frac{s}{L_\delta(s+\alpha_b)^2}F_E(s) \end{aligned} \quad (21)$$

It can be seen from Equation (21) that  $Y(s) = R(s)$  at steady-state and the CW currents converge to the reference value  $R(s)$ , the second term of Equation (21) is trivial and equals to zero in steady state by selecting a suitable  $\alpha_b$ , thus the proposed method achieves the control goal and has the anti-disturbance ability.

### 3.2. Controller Parameters Design

In order to guarantee that the CW current sub-system has a faster timescale dynamics than that of the flux sub-system, the bandwidth of the current controller is designed much larger than the real parts of the flux sub-system poles. However, the large  $\alpha_b$  achieves a good tracking performance, while the control performance is susceptible to disturbance. In this case, the bandwidth is designed as:

$$\alpha_b \geq 10\delta \quad (22)$$

On the other hand, the PW flux and PW voltage are constant within the timescale of the CW current sub-system, consequently the CW current sub-system behaves as a first-order system, where the time constant is  $1/\alpha_b$ . In order to obtain well control performance, the bandwidth  $\alpha_b$  is related to the 10–90% of the rise time  $t_{rc}$  and  $\alpha_b t_{rc} = \ln 9 \approx 2.2$ .

In practice, the control method is implemented in the discrete-time system, where the bandwidth should be smaller than the sampling angular frequency  $\omega_{samp}$  [28], so as to avoid the interference caused by the high-frequency PWM signals. In this paper, the upper bound of  $\alpha_b$  is:

$$\alpha_b \leq \frac{\omega_{samp}}{10} \quad (23)$$

### 3.3. Controller Design at the Symmetrical PW Voltage Sag Case

Since the flux sub-system shows the slow timescale dynamic feature, the EMF term  $F_E$  is divided into two parts within the timescale of the current sub-system as  $E_{slow}$  and  $E_{fast}$ , and  $E_{slow} = a_{12} \begin{bmatrix} \varphi_{pd}(s) & \varphi_{pq}(s) \end{bmatrix}^T + a_{13} \begin{bmatrix} \varphi_{rd}(s) & \varphi_{rq}(s) \end{bmatrix}^T$ ,  $E_{fast} = w_{11} \begin{bmatrix} v_{pd}(s) & v_{pq}(s) \end{bmatrix}^T$ , where the fluxes and the PW voltage are the quasi-constant. In order to compensate the disturbance caused by the voltage sags,  $\hat{w}_{11} \begin{bmatrix} v_{pd}(s) & v_{pq}(s) \end{bmatrix}^T$  is added to the feedforward components, where “ $\hat{w}_{11}$ ” is the estimated value of  $w_{11}$ . Therefore, the improved CW current regulator is designed as:

$$U(s) = \hat{G}^{-1}(s)Y(s) - F_R Y(s) + F_{PI}(s)E(s) - \hat{w}_{11} \begin{bmatrix} v_{pd}(s) & v_{pq}(s) \end{bmatrix}^T \quad (24)$$

when the parameters match and  $\hat{w}_{11} = w_{11}$ , from Equations (15) and (24), the CW current is calculated as:

$$Y(s) = L_R(s)R(s) + L_E(s)E_{slow}(s) \quad (25)$$

Similarly, since the fluxes are considered as constant within a current control period, the CW current tracks the reference value in the steady state, and the tracking error approaches zero. Finally, the overall diagram of the current controller is given in Figure 3, where it consists of the internal model current controller in Equation (18), the active damping controller in Equation (19), and the feedback term composed by the PW voltage. Considering that the expected rotor speeds and power both are achieved by adjusting the CW stator current, and these outer loop control methods can refer to the existing references as discussed in Section 1, thus only the inner current controller is addressed and verified in this paper.

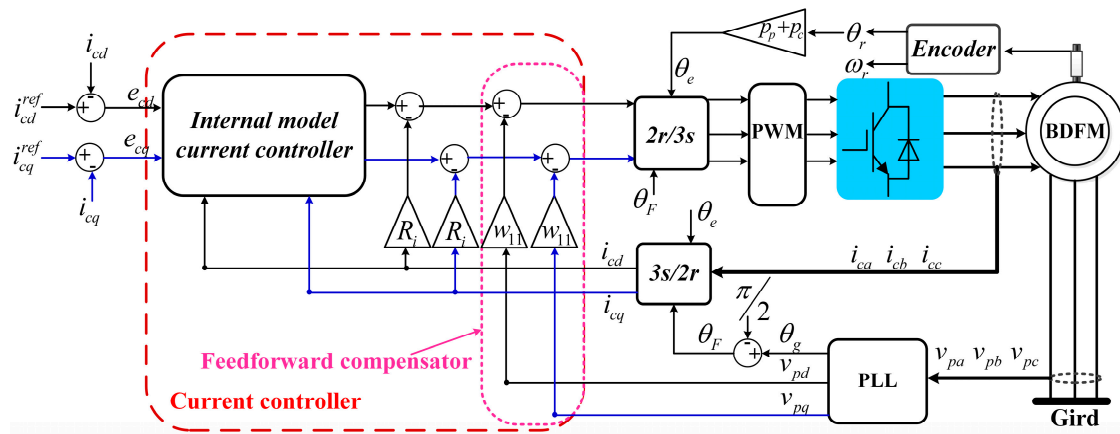


**Figure 3.** Schematic diagram for the CW current control of the brushless doubly-fed induction machine drive system.

#### 4. Parameter Estimation and Its Influence on Control Performance

From Equations (18), (19) and (24), a good control performance is guaranteed by three parameters: the total leakage inductance  $L_\sigma$ , the total resistance  $R_t$ , and  $w_{11}$ , which are related to the motor parameters. Therefore, these parameters are measured and the parametric errors on the control performance are analyzed.

##### 4.1. Parameter Estimation

As described in the Appendix A,  $L_\sigma$  is complex to calculate and it relates to many motor parameters, where some of them are difficult to directly obtain. Since the leakage inductances of the PW stator, CW stator, and rotor, denoted as  $L_{1p}$ ,  $L_{1c}$ , and  $L_{1r}$ , are much smaller compared with the self-inductance and mutual inductance,  $\hat{L}_\delta$  takes the second-order Taylor series expansion of  $L_\sigma$  at  $L_{1p} = L_{1c} = L_{1r} = 0$  so as to simplify the estimation of  $L_\sigma$ , and then  $\hat{L}_\delta$  is expressed as:

$$\hat{L}_\sigma = L_{1p} + L_{1r} + L_{1c} \tag{26}$$

Similarly, since  $R_t$  is larger than the leakage inductances, the first-order Taylor series expansion of  $R_t$  around  $L_{1p} = L_{1c} = L_{1r} = 0$  is used to obtain  $\hat{R}_t$ , which is expressed as:

$$\hat{R}_t = R_p + R_c + R_r \tag{27}$$

Meanwhile,  $\hat{w}_{11}$  is calculated as the first-order Taylor series expansion of  $w_{11}$  around  $L_{1p} = L_{1c} = L_{1r} = 0$ , which leads to:

$$\hat{w}_{11} = 1 \tag{28}$$

It can be seen from the above analyses that  $\hat{R}_t$  and  $\hat{L}_\delta$  are obtained as the sum of the leakage inductances and the sum of the resistances, which are measured from the single-equivalent phase of the BDFIM shown in Figure 4. The high-frequency AC voltage source is connected to the PW terminals

of the BDFIM, and the CW terminals are in short-circuit case, where the applied power source can be provided by the power converter or an impedance analyzer. Because the impedance of  $M_p$  and  $M_c$  are much larger than the leakage inductance, the mutual inductance path is considered as open-circuited, which is illustrated by the dashed lines in Figure 4. Consequently, the equivalent impedance is equal to  $\hat{R}_t + j\omega_{ac}\hat{L}_\delta$ , where  $\omega_{ac}$  is the electric angular frequency of the AC source. Referring to the Circuit Theory,  $\hat{R}_t$  and  $\hat{L}_\delta$  are calculated by the amplitude and the phase of the excited current and the voltage of the applied AC power source.

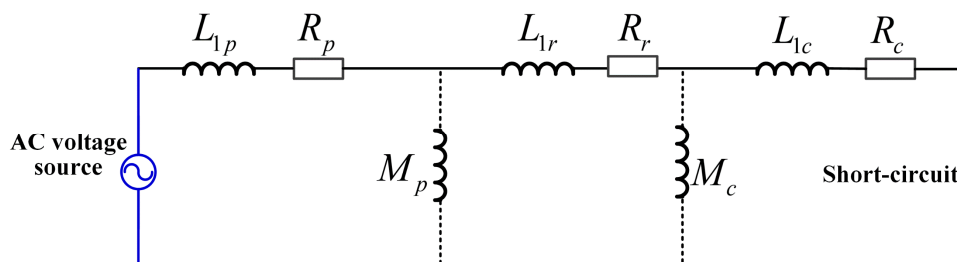


**Figure 4.** Measure circuit diagram of a single-equivalent phase of the brushless doubly-fed induction machine.

#### 4.2. Effects of the Parametric Errors on Control Performance

As discussed above, the total resistance  $R_t$  and the total leakage inductance  $L_\sigma$  are the main factors affecting the control performance, because  $w_{11}$  is approximately constant. For  $R_t$ , the active resistance  $R_i$  is incorporated in the current control to suppress its influence, where  $R_i$  is designed as  $R_i \geq 5R_t$  here. Combing with Equation (19), when the bandwidth  $\alpha_b$  satisfies Equation (29), the parameter error of  $R_t$  has no effects on the control performance:

$$\alpha_b \geq \frac{5\hat{R}_t}{\hat{L}_\delta} \quad (29)$$

In terms of  $L_\delta$ , assuming that  $\hat{L}_\delta$  matches  $L_\delta$  and the parameter error is defined as  $\tilde{L}_\delta = \hat{L}_\delta - L_\delta$ , the CW current in Equation (21) is derived by estimating  $\tilde{L}_\delta$  as the first-order Taylor series expansion of  $\tilde{L}_\delta$  at  $\tilde{L}_\delta = 0$ , which is expressed as:

$$Y(s) = \left( \frac{a_b}{a_b + s} + \tilde{L}_\sigma \frac{a_b s(s + j\omega_{slc})}{L_\sigma (a_b + s)^3} \right) R(s) + \left( \frac{s}{L_\sigma (a_b + s)^2} - \tilde{L}_\sigma \frac{s(a_b^2 + 2a_b s + j\omega_{slc} s)}{L_\sigma^2 (a_b + s)^4} \right) F_E(s) \quad (30)$$

It can be seen from Equation (30) that the CW current tracks the reference value at steady state and effects of  $\tilde{L}_\delta$  are eliminated, since  $Y(s) = R(s)$  when the time approaches infinity according to the Final Value Theorem. Thus, the small parametric error of the leakage inductance does not influence the poles' location of the CW current sub-system, consequently the dynamic performance is not significantly influenced.

## 5. Simulation and Experimental Result

### 5.1. Simulation

In order to evaluate the correctness of the proposed CW current control method, a 30 kW BDFIM system is established in the MATLAB/Simulink platform (MATLAB 7.0), where the machine parameters are listed in Table 1. The total resistance and the total leakage inductance are 1.63183  $\Omega$  and 0.0147 H, which are calculated by the computer numerical simulations. In the current controller,

the sampling frequency  $f_{samp}$  of the control loop is 4 kHz, the controller parameters are designed based on the calculations of (22), (23) and (29) as discussed in Sections 3.2 and 4.2, the bandwidth  $\alpha_b$  is designed as  $300\pi$  rad/s on the basis of the BDFIM parameters, while the rise time  $t_{rc}$  is 2.33 ms. In order to prevent the integrator windup in the over modulation range, the integrators of PI controllers are updated by a modified error, which is the “back-calculated” error [29].

**Table 1.** Parameters of 30 kW BDFIM provided by manufacturer.

Parameter	Value	Parameter	Value
$M_p$	0.4663 H	PW rated voltage	380 V/50 Hz
$M_c$	0.0488 H	Rated power	30 KW
$L_p$	0.4706 H	PW poles	2
$L_c$	0.0510 H	CW poles	6
$L_r$	0.5233 H	Natural speed	750 rpm
$R_r$	0.78524 $\Omega$	$J$	0.95 kgm <sup>2</sup>
$R_p$	0.40355 $\Omega$	DC-link voltage	650 V
$R_c$	0.44304 $\Omega$		

### 5.1.1. Dynamic Responses

In this case, the  $q$ -axis reference current  $i_{cq}^{ref}$  changes from 0 A to 63 A, and then it decreases from 63 A to 0 A, where the BDFIM is entirely magnetized from the CW stator side. Figure 5 shows the simulation results of the CW current at different rotor speeds respectively. The 500 rpm, 750 rpm, and 1000 rpm lines correspond to the sub-synchronous mode, synchronous mode, and sup-synchronous mode of the BDFIM, respectively. The rise time of the CW current mainly depends on the designed values, but it is slightly affected at various speeds, and the current  $i_{cq}$  takes a long time to track the reference value at the high rotor speed. This is because that the CW output voltage saturates during the transient process at various speeds, due to the limit of the dc-link-voltage.

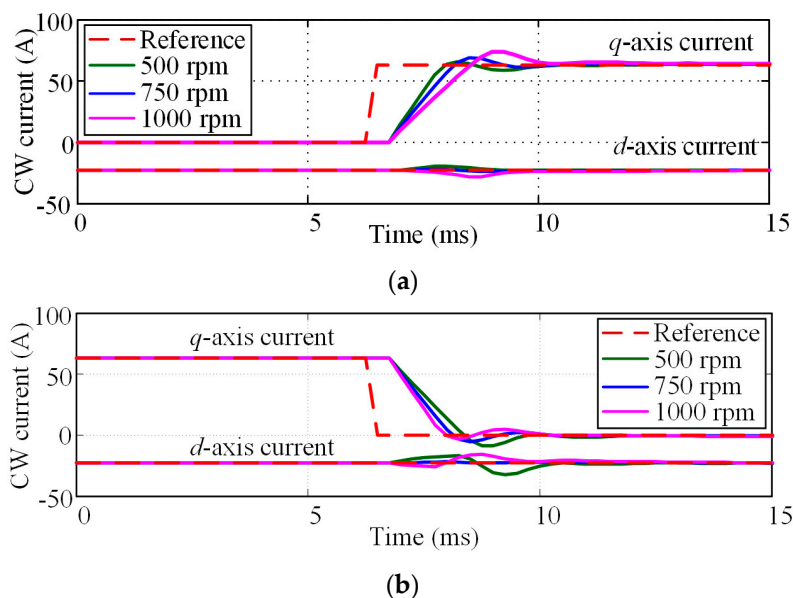


**Figure 5.** Dynamic responses of the CW current at different speeds (measure (solid); reference (dashed)). (a)  $i_{cq}$  changes from 0 A to 63 A; (b)  $i_{cq}$  decrease from 63 A to 0 A.

Furthermore, as shown in Figure 6a, when the DC-link voltage is high enough and it does not affect the output voltage of the power converter, an equal rise time of the current controller is achieved, and the dynamic response of CW currents at different speeds are same. However, there is a slight



fluctuation since the sampling frequency  $f_{samp}$  of the control loop is low. When  $f_{samp}$  increases to 20 kHz, the fluctuation of the CW  $q$ -axis currents vanishes as shown in Figure 6b.

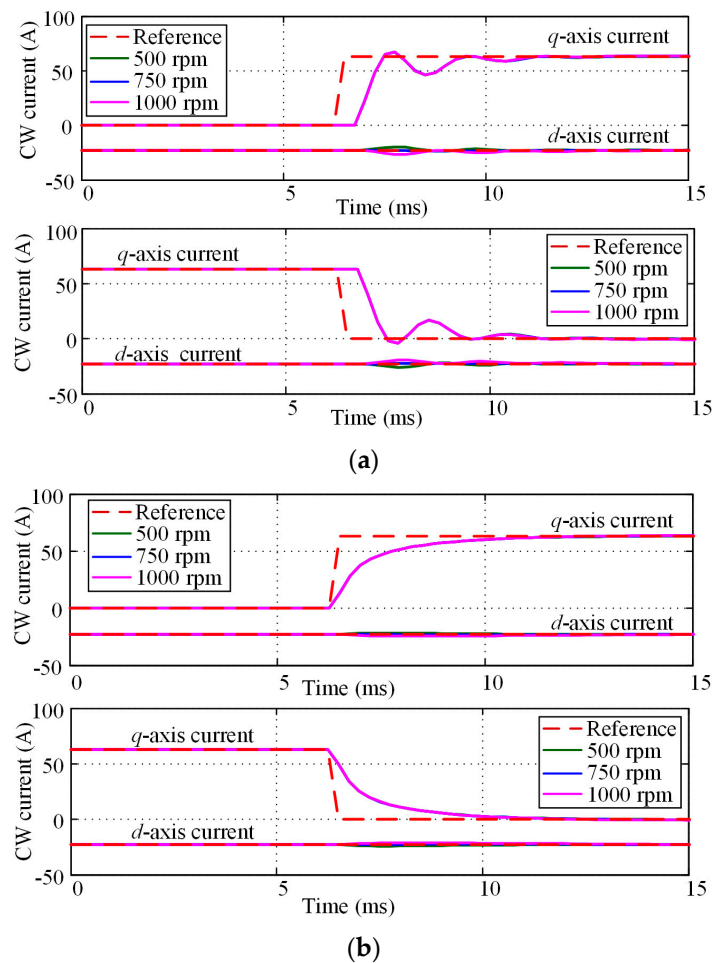


**Figure 6.** Dynamic responses of the CW current at different speeds (measure (solid); reference (dashed)). (a)  $f_{samp}$  is 4 kHz; (b)  $f_{samp}$  is 20 kHz.

### 5.1.2. Control Performance with Different Estimated Parameters

Figure 7 illustrates the dynamic responses of the CW currents with different estimated parameters at 750 rpm, where the cases of the estimation errors of  $\pm 20\%$  of the total resistance  $\hat{R}_t$  and the total leakage inductance  $\hat{L}_\delta$  are discussed. In Figure 8a, the  $q$ -axis CW current reference changes from 0 A to 63 A, where the zoom-in waveforms of  $i_{cq}$  are given in the lower figure. Also, the transient response when it changes from 63 A to 0 A is shown in Figure 8b. It can be seen that the parametric error of the estimated total resistance  $\hat{R}_t$  has tiny effects on the dynamic responses of the CW currents, while large overshoots are generated for the case with parametric errors of the total leakage inductance  $\hat{L}_\delta$ . However, because the poles' location of the CW current sub-system, the estimation errors of  $\hat{R}_t$  and  $\hat{L}_\delta$  have slight impacts on the rise time of the CW current responses.

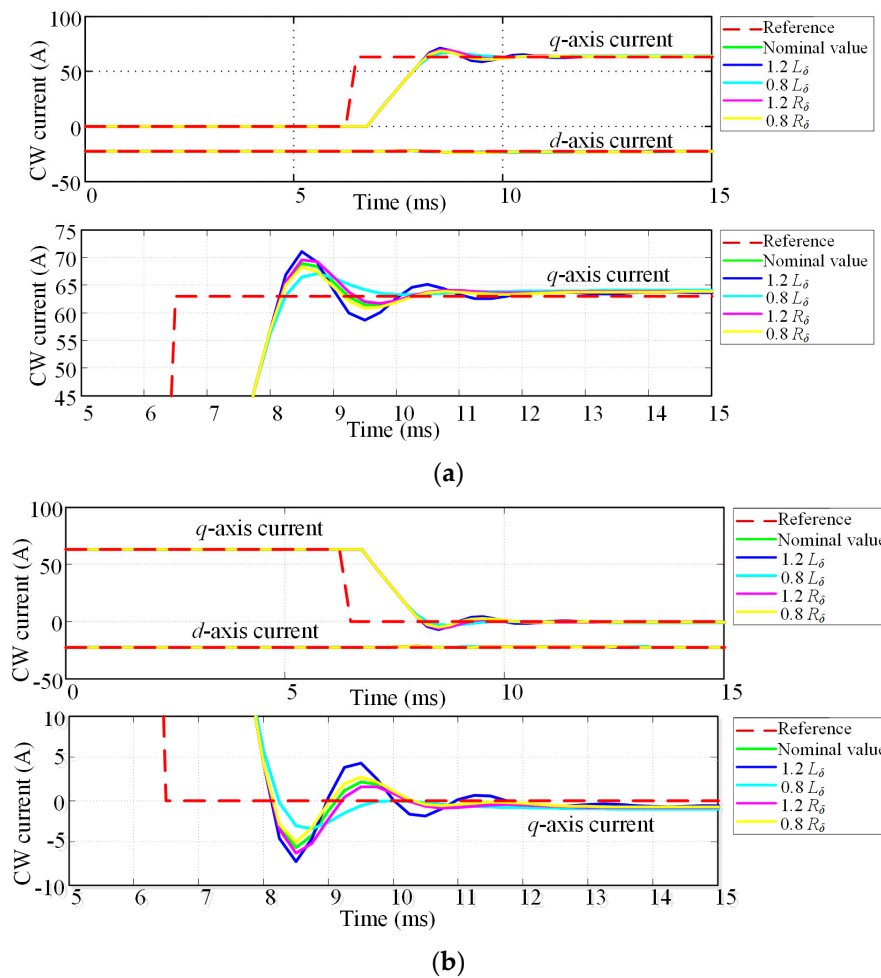


**Figure 7.** Dynamic responses of the CW currents with different estimated parameters at 750 rpm (measure (solid); reference (dashed)). (a)  $i_{cq}$  changes from 0 A to 63 A; (b)  $i_{cq}$  decreases from 63 A to 0 A.

### 5.1.3. Dynamic Responses with Symmetrical Voltage Sags

The case when the PW voltages symmetrically drop to zero is studied, where the rotor speed is 500 rpm and  $i_{cq}^{ref}$  is 63 A. The control performance of the feedback control in the proposed controller is shown in Figure 8a, and a zoom-in waveform of  $i_{cq}$  is given in Figure 8b. When the PW voltage sags happen, the reference current  $i_{cq}^{ref}$  changes to 0 A, and fluctuations of the CW q-axis current without the PW voltage feedforward is almost two times larger than that with the PW voltage feedforward control. In this case, the proposed method achieves a good dynamic response.

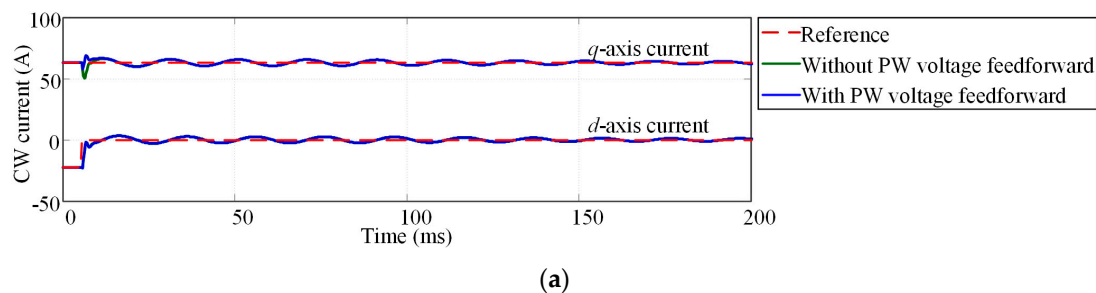


**Figure 8.** Cont.

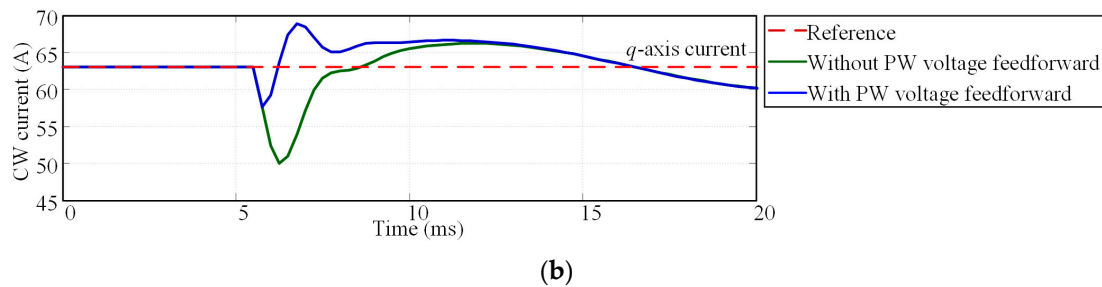


**Figure 8.** Dynamic responses of the CW currents at 500 rpm when the PW voltages symmetrically sag (Measure (solid); reference (dashed)). (a) Waveforms within 200 ms; (b) zoom-in waveforms within 20 ms.

## 5.2. Experimental Results

Figure 9 shows the experimental rig of the BDFIM system, the PW stator of the BDFIM is directly connected to the power grid (380 V/50 Hz), and the CW stator of the BDFIM is fed by a PWM inverter, and more details are discussed in [25]. The CW current control algorithm is implemented by the digital signal processor (DSP, TMS32028335), and the field-programmable gate array (FPGA, EP2C8J144C8N) generates the drive signals for the insulated gate bipolar transistor (IGBT). The total resistance and the total leakage inductance are measured by an impedance analyzer, which are 1.63183  $\Omega$  and 0.009 H, respectively.

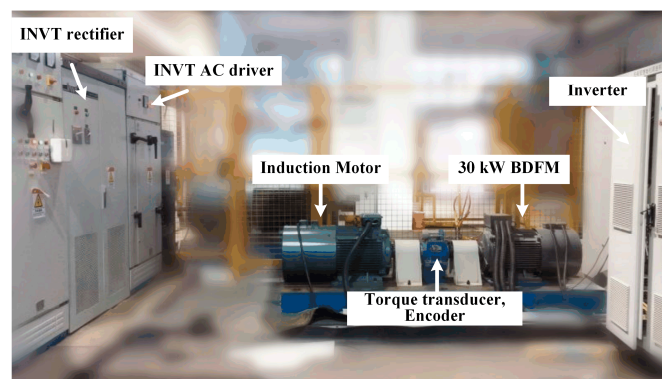


**Figure 9.** The brushless doubly-fed induction machine test rig.

Figure 10 shows the dynamic waveforms of the CW currents at the rotor speeds of 500 rpm, 750 rpm, 1000 rpm, and the parameters of the controller are same as that in the simulation. It can be seen that the rise time of the CW currents at high rotor speed is larger than that of the low speed, which is consistent with the simulation results. Because the estimated motor parameters have slight errors compared with the practical parameters, the currents have larger fluctuations than the simulation. However, these can be eliminated by increasing the sampling frequency as discussed above. Furthermore, due to the limit of the DC-link voltage, the CW voltage may be saturated during the adjusted process. Consequently, the rise time of CW current at various speeds are slightly different.

Subsequently, the effects of motor parametric errors on the control performance are studied. Figure 11 illustrates the experimental results of dynamic responses of the CW current at 750 rpm, and the zoom-in waveforms of  $i_{cq}$  are given in the lower figure. When the motor parameters have 20% errors, the controller can adjust the CW currents to reach the expected values, and the robustness of the controller is verified. Also, the rise time at different parametric errors has slight difference, since the CW current dynamic has the same poles. On the other hand, it can be seen from the zoom-in waveforms that the dynamic performance is worse when the total leakage inductance  $\hat{L}_\delta$  has parametric

errors, compared with the case that the total resistance  $\hat{R}_t$  has  $\pm 20\%$  errors, and the overshoots of CW currents are large at  $1.2 \hat{L}_\delta$ . In this case, the estimated total resistance  $\hat{R}_t$  has fewer effects on the dynamic responses of the CW currents than that of the estimated total leakage inductance, since the active damping terms are incorporated in the proposed method.

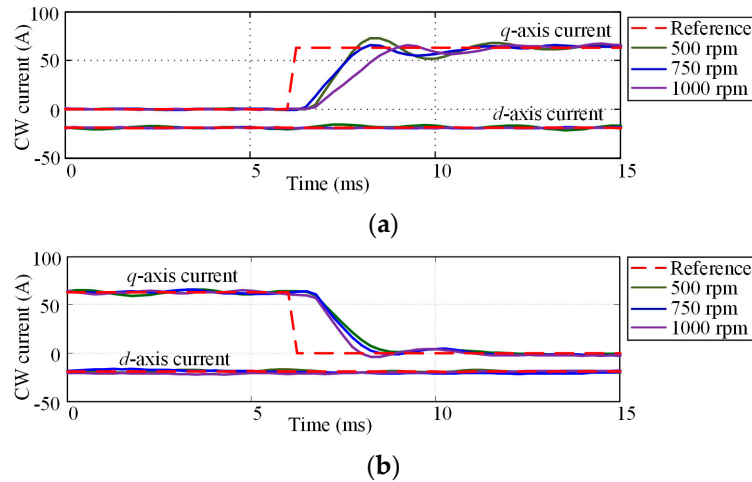


**Figure 10.** Dynamic responses of the CW current at different speeds (measure (solid); reference (dashed)). (a)  $i_{cq}$  changes from 0 A to 63 A; (b)  $i_{cq}$  decreases from 63 A to 0 A.

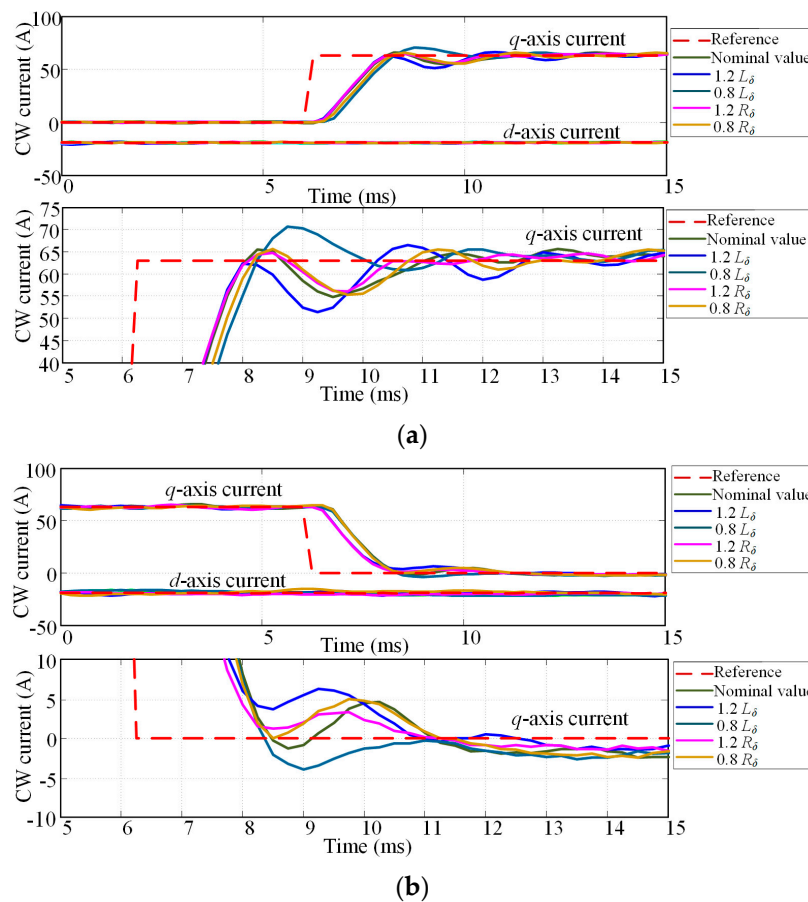


**Figure 11.** Dynamic responses of the CW current with different estimated parameters at 750 rpm (measure (solid); reference (dashed)). (a)  $i_{cq}$  changes from 0 A to 63 A; (b)  $i_{cq}$  decreases from 63 A to 0 A.

## 6. Discussion

In this part, the feasibility of the proposed method is further discussed, the comparison between the proposed method and the conventional method is conducted, and its practicality is verified by generating the expected CW currents with wind speed data.

### 6.1. Comparisons between the Proposed Method and the Conventional Control Method

Compared with the PI controller in [18], the controller parameters are related to the easily measured values of the total resistance and the total inductance, while it takes a lot of effort to adjust the controller parameters of the conventional methods by trial and error methods; the proposed method eliminates the complex feedforward terms composed by the motor parameters and variables, which achieves fast-dynamic response and greatly reduces the effects caused by the parametric errors.

Figure 12 shows simulation results with the proposed method and the PI control methods using different feedforward terms at 900 rpm, where the current reference  $i_{cq}^{ref}$  changes between 20 A, 30 A, 40 A and 50 A at 2.0 s, 2.5 s, and 3.0 s, respectively. In PI-1, PI-2 and PI-3 methods, no feedforward term, feedforward terms composed by the CW currents and the PW flux in steady state, feedforward terms consisting of CW currents are added in the controller, respectively. It can be seen from Figure 12 that the overshoot amplitudes with the proposed method are about 2 A, which is much smaller than that of the other methods, the proposed method quickly achieves the reference value, where the long time is required to reach the steady state in other methods. In addition, a good control performance is achieved when the feedforward term is composed by the relatively accurate EMF term. Therefore, the proposed method has the faster dynamic response and well steady state performance, which has the ability to quickly track the current reference.

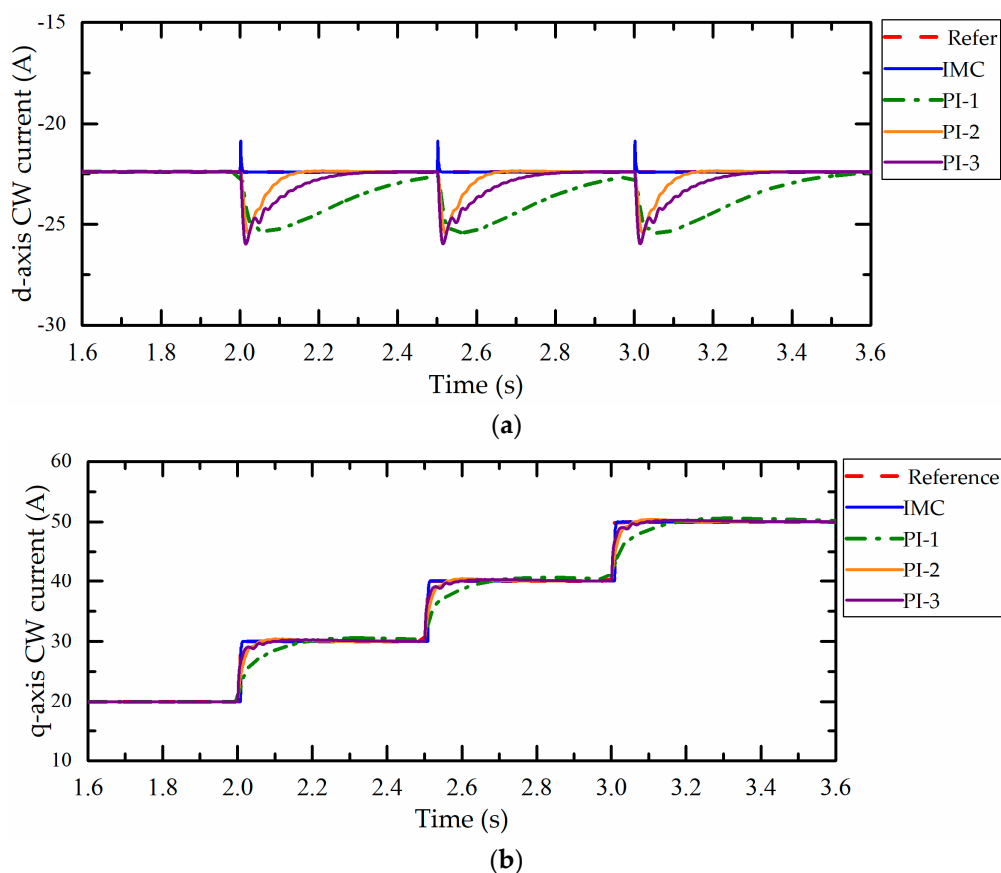


**Figure 12.** Dynamic responses of the CW current with different control methods. (a)  $i_{cd}$ ; (b)  $i_{cq}$ .

## 6.2. Dynamic Performance with Variable Wind Speeds

In practice, the wind speed fluctuates with time, and a series of wind speed data is shown in Figure 13, where the sampling time is one second. In the WEGs, assuming that the cut-in wind speed is 4 m/s, the cut-out wind speed is 25 m/s and the rated wind speed is 12 m/s, thus the output power of the BDFIM is time-varying because of the fluctuations of the wind speed. Consequently, when the BDFIM works in the WEGs, the CW current reference obtained from the outer loop of the power or the rotor speed changes with time. According to [30], wind speeds lead to different rotor speeds at different operation modes. In order to clearly discuss the feasibility of the proposed method in the WEGs, two scenarios when the wind speed is below the rated wind speed (denoted as Case I) and the speed is below and above the rated wind speed (denoted as Case II) are studied in this paper, but it should be noted that the proposed method is capable of operating at any wind speed as given in Figure 13. Assuming that the output power follows the maximum power point tracking method, the rotor speed varies with the wind speed in case I so as to obtain the maximum output power; while the output power achieves the rated value when the wind speed is higher than 12 m/s.

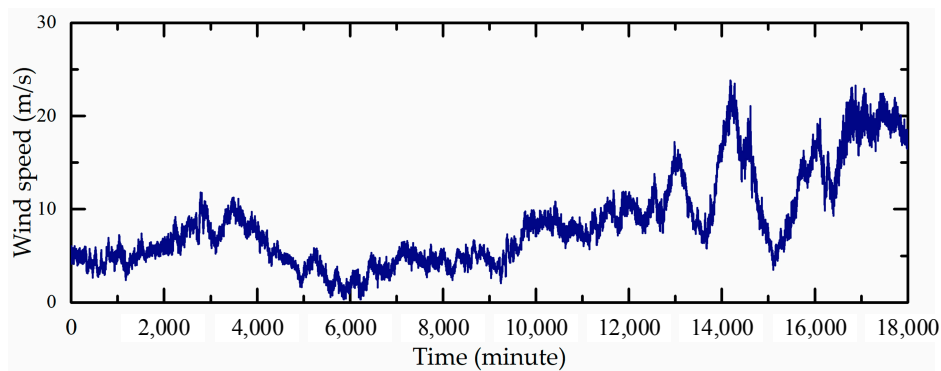


Figure 13. The wind speed series with the sample time of one second.

Figure 14 shows the CW current waveforms with the proposed method in Case I, the output power varies with the wind speeds to achieve a maximum value, consequently the  $q$ -axis current reference changes with the wind speeds, where the  $d$ -axis current reference is constant to guarantee zero reactive power. It can be seen that the CW currents have overshoots within 0.5 A when the wind speed changes, and they quickly reach the steady state with tiny tracking errors. In Case II, the output power achieves the rated value when the wind speed is higher than 12 m/s, the  $q$ -axis current reference reaches the maximum value, and the CW currents are shown in Figure 15. Similarly, the  $q$ -axis current tracks the references when the wind speed changes, while the  $d$ -axis current shows the short-time fluctuations, where the overshoots are within 2 A, and it quickly achieves the steady state. Since the fluctuations of the wind speed are higher in Figure 15, the variations of the CW currents are larger, especially the  $d$ -axis CW currents. Compared with Figure 14,  $i_{cq}$  keeps the maximum value at some wind speeds as given at  $t = 30$  s, while the CW currents track the references and they are adjusted with the wind speeds in both two cases. Therefore, the proposed method is able to be used in the WEGs, which achieves a good dynamic performance and the tracking errors are tiny.

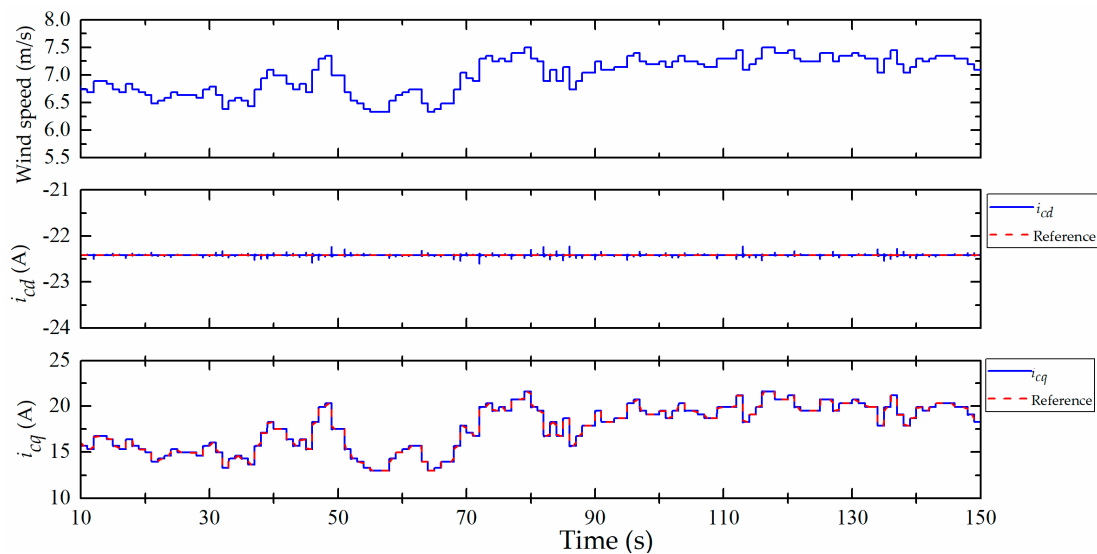


Figure 14. Dynamic responses of the CW currents in Case I.

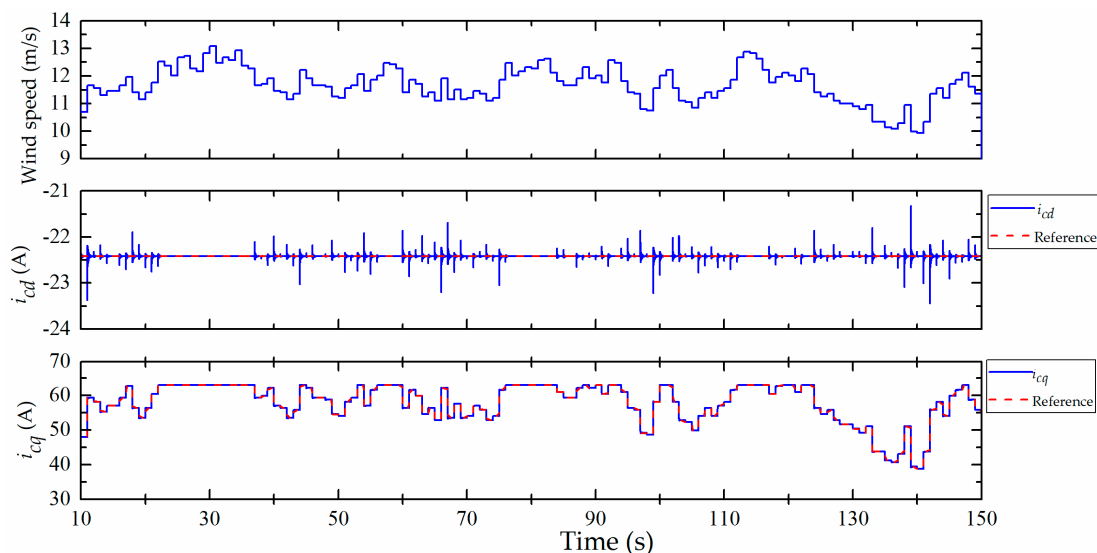


Figure 15. Dynamic responses of the CW currents in Case II.

## 7. Conclusions

In this paper, a state-space mathematical model of the BDFIM is established by selecting the PW flux, the rotor flux and the CW current as state variables, the slow dynamic characteristics of the flux sub-system is analyzed, and then the current sub-system is independently designed. In order to eliminate the effects of coupling terms and the parametric errors on the control performance, the internal model current control method with an active damping controller is proposed. Compared with the conventional method, the proposed method simplifies the design of controller parameters, it achieves a fast-dynamic response by designing a suitable bandwidth of the current controller when the rotor speed is variable and the current references change. Furthermore, the feedforward compensator composed by the EMF is studied when the PW voltage sags. The simulation and experimental results verify the correctness and feasibility of the proposed method, and the control performance is slightly affected by the erroneous parameters.

**Author Contributions:** All authors have worked on this manuscript together and all authors have read and approved the final manuscript.



**Funding:** This work was supported by the National Natural Science Foundation of China under Grants 51677195.

**Conflicts of Interest:** The authors declare no conflicts of interest.

## Appendix A

Coefficients of the state-space mathematical model of the BDFIM are listed as:  
 $K_\delta = \frac{1}{L_r L_p - M_p^2}$ ,  $L_\sigma = K_\delta (L_r L_c L_p - L_p M_c^2 - L_c M_p^2)$ ,  $R_t = K_\delta^2 M_c^2 (R_p M_p^2 + R_r L_p^2) + R_c$ ,  $w_{11} = K_\delta M_c M_p$ ,  
 $a_{12} = -K_\delta^2 M_c M_p (L_r R_p + L_p R_r) - j(P_c + P_p) \omega_r K_\delta M_c M_p$ ,  $a_{13} = K_\delta^2 M_c (M_p^2 R_p + L_p^2 R_r) + j P_p \omega_r K_\delta L_p M_c$ ,  
 $a_{21} = -K_\delta M_c M_p R_p$ ,  $a_{22} = K_\delta L_r R_p$ ,  $a_{23} = K_\delta M_p R_p$ ,  $a_{31} = K_\delta M_c L_p R_r$ ,  $a_{32} = K_\delta M_p R_r$ ,  $a_{33} = K_\delta L_p R_r$ .

## References

1. Song, D.; Yang, J.; Fan, X.; Liu, Y.; Liu, A.; Chen, G.; Joo, Y.H. Maximum power extraction for wind turbines through a novel yaw control solution using predicted wind directions. *Energy Convers. Manag.* **2018**, *157*, 587–599. [[CrossRef](#)]
2. Yaramasu, V.; Wu, B.; Sen, P.C.; Kouro, S.; Narimani, M. High-Power Wind Energy Conversion Systems: State-of-the-Art and Emerging Technologies. *Proc. IEEE* **2015**, *103*, 740–788. [[CrossRef](#)]
3. Williamson, S.; Ferreira, A.C.; Wallace, A.K. Generalised theory of the brushless doubly-fed machine. I. Analysis. *IEE Proc.-Electr. Power Appl.* **1997**, *144*, 111–122. [[CrossRef](#)]
4. Zheng, P.; Wu, Q.; Zhao, J.; Tong, C.; Bai, J.; Zhao, Q. Performance Analysis and Simulation of a Novel Brushless Double Rotor Machine for Power-Split HEV Applications. *Energies* **2012**, *5*, 119–137. [[CrossRef](#)]
5. Xiong, F.; Wang, X. Design of a low-harmonic-content wound rotor for the brushless doubly fed generator. *IEEE Trans. Energy Convers.* **2014**, *29*, 158–168. [[CrossRef](#)]
6. Ou, L.; Wang, X.; Xiong, F.; Ye, C. Reduction of torque ripple in a wound-rotor brushless doubly-fed machine by using the tooth notching. *IET Electr. Power Appl.* **2018**, *12*, 635–642. [[CrossRef](#)]
7. Peng, H.; Cheng, M.; Luo, R. Design and Analysis of a Brushless Doubly-Fed Induction Machine With Dual-Stator Structure. *IEEE Trans. Energy Convers.* **2016**, *31*, 1132–1141.
8. Xia, C.; Hou, X. Study on the Static Load Capacity and Synthetic Vector Direct Torque Control of Brushless Doubly Fed Machines. *Energies* **2016**, *11*, 966. [[CrossRef](#)]
9. Strous, T.D.; Polinder, H.; Ferreira, J.A. Brushless doubly-fed induction machines for wind turbines: Developments and research challenges. *IET Electr. Power Appl.* **2017**, *11*, 991–1000. [[CrossRef](#)]
10. Sarasola, I.; Poza, J.; Oyarbide, E.; Rodríguez, M.Á. Stability analysis of a brushless doubly-fed machine under closed loop scalar current control. In Proceedings of the IECON 2006-32nd Annual Conference on IEEE Industrial Electronics, Paris, France, 6–10 November 2006; pp. 1527–1532.
11. Hu, J.; Zhu, J.; Dorrell, D.G. A new control method of cascaded brushless doubly fed induction generators using direct power control. *IEEE Trans. Energy Convers.* **2014**, *29*, 771–779. [[CrossRef](#)]
12. Zhao, R.; Zhang, A.; Ma, Y.; Wang, X.; Yan, J.; Ma, Z. The dynamic control of reactive power for the brushless doubly fed induction machine with indirect stator-quantities control scheme. *IEEE Trans. Power Electron.* **2015**, *30*, 5046–5057. [[CrossRef](#)]
13. Sarasola, I.; Poza, J.; Rodríguez, M.A.; Abad, G. Direct torque control design and experimental evaluation for the brushless doubly fed machine. *Energy Convers. Manag.* **2011**, *52*, 1226–1234. [[CrossRef](#)]
14. Li, K.; Huang, S. Direct Flux Control for Stand-Alone Operation Brushless Doubly Fed Induction Generators Using a Resonant-Based Sliding-Mode Control Approach. *Energies* **2018**, *11*, 814.
15. Xia, C.; Ho, X.; Chen, F. Flux-Angle-Difference Feedback Control for the Brushless Doubly Fed Machine. *Energies* **2018**, *11*, 1–16.
16. Shao, S.; Abdi, E.; Barati, F.; McMahon, R. Stator-flux-oriented vector control for brushless doubly fed induction generator. *IEEE Trans. Ind. Electron.* **2009**, *56*, 4220–4228. [[CrossRef](#)]
17. Protsenko, K.; Xu, D. Modeling and control of brushless doubly-fed induction generators in wind energy applications. *IEEE Trans. Power Electron.* **2008**, *23*, 1191–1197. [[CrossRef](#)]
18. Poza, J.; Oyarbide, E.; Sarasola, I.; Rodríguez, M. Vector control design and experimental evaluation for the brushless doubly fed machine. *IET Electr. Power Appl.* **2009**, *3*, 247–256. [[CrossRef](#)]

19. Liu, Y.; Ai, W.; Chen, B.; Chen, K.; Luo, G. Control design and experimental verification of the brushless doubly-fed machine for stand-alone power generation applications. *IET Electr. Power Appl.* **2016**, *10*, 25–35. [[CrossRef](#)]
20. Tohidi, S. Analysis and simplified modelling of brushless doubly-fed induction machine in synchronous mode of operation. *IET Electr. Power Appl.* **2016**, *10*, 110–116. [[CrossRef](#)]
21. Tohidi, S.; Oraee, H.; Zolghadri, M.R.; Shao, S.; Tavner, P. Analysis and enhancement of low-voltage ride-through capability of brushless doubly fed induction generator. *IEEE Trans. Ind. Electron.* **2013**, *60*, 1146–1155. [[CrossRef](#)]
22. Long, T.; Shao, S.; Abdi, E.; McMahon, R.A.; Liu, S. Asymmetrical low-voltage ride through of brushless doubly fed induction generators for the wind power generation. *IEEE Trans. Energy Convers.* **2013**, *28*, 502–511. [[CrossRef](#)]
23. Chen, J.; Zhang, W.; Chen, B.; Ma, Y. Improved Vector Control of Brushless Doubly Fed Induction Generator under Unbalanced Grid Conditions for Offshore Wind Power Generation. *IEEE Trans. Energy Convers.* **2016**, *31*, 293–302. [[CrossRef](#)]
24. Petersson, A.; Harnefors, L.; Thiringer, T. Comparison between stator-flux and grid-flux-oriented rotor current control of doubly-fed induction generators. In Proceedings of the 2004 IEEE 35th Annual Power Electronics Specialists Conference, Aachen, Germany, 20–25 June 2004; pp. 482–486.
25. Yang, J.; Tang, W.; Zhang, G.; Sun, Y.; Ademi, S.; Blaabjerg, F.; Zhu, Q. Sensorless Control of Brushless Doubly-Fed Induction Machine Using a Control Winding Current MRAS Observer. *Trans. Ind. Electron.* **2018**. [[CrossRef](#)]
26. Barati, F.; McMahon, R.; Shao, S. Generalized vector control for brushless doubly fed machines with nested-loop rotor. *IEEE Trans. Ind. Electron.* **2013**, *6*, 2477–2485. [[CrossRef](#)]
27. Harnefors, L.; Nee, H.P. Model-based current control of AC machines using the internal model control method. *IEEE Trans. Ind. Appl.* **1998**, *34*, 133–141. [[CrossRef](#)]
28. Sul, S.K. *Control of Electric Machine Drive Systems*; John Wiley & Sons: Hoboken, NJ, USA, 2011.
29. Harnefors, L.; Pietilainen, K.; Gertmar, L. Torque-maximizing field-weakening control: Design, analysis, and parameter selection. *IEEE Trans. Ind. Electron.* **2005**, *48*, 161–168. [[CrossRef](#)]
30. Burton, T.; Jenkins, N.; Sharpe, D.; Bossanyi, E. *The Wind Resource, in Wind Energy Handbook*; John Wiley & Sons, Ltd.: Chichester, UK, 2001.



© 2018 by the authors. Licensee MDPI, Basel, Switzerland. This article is an open access article distributed under the terms and conditions of the Creative Commons Attribution (CC BY) license (<http://creativecommons.org/licenses/by/4.0/>).